Thermochemical Nonequilibrium Issues for Earth Re-Entry of Mars Mission Vehicles

R. A. Mitcheltree* and P. A. Gnoffo†
NASA Langley Research Center, Hampton, Virginia 23665

The thermochemical environment about an axisymmetric 60-deg sphere cone with a circular aft skirt is computed using the NASA Langley Aerothermodynamic Upwind Relaxation Algorithm. Earth entry at 12 km/s is examined at 70- and 80-km altitude for two vehicle base radii of 2 and 6 m. These four test cases bracket some proposed scenarios for Earth re-entry of a manned Mars mission aerobrake at this velocity. Thermochemical nonequilibrium results are examined for each case and compared with thermal equilibrium results produced by artificially accelerating vibrational relaxation rates and with equilibrium results produced by a viscous shock layer method. The thermal and chemical nonequilibrium effects present in the four cases range from minimal in the largest body at 70-km altitude to dominant in the smaller body at 80-km altitude.

Nomenclature

D = Damkohler number
R = nose radius, m
T = heavy particle translational temperature, K
T_V = vibrational electronic electron-translational temperature, K
x,z = spatial coordinates, m
η/η_{sh} = normal distance from body over shock standoff distance
ρ_{O_2} = specific density of molecular oxygen, kg/m^3
ρ_∞ = freestream density, kg/m^3
τ_c = characteristic time scale for the chemical reactions, s
τ_f = characteristic time scale for the flow, s
τ_v = characteristic time scale for the vibrational relaxation, s

Introduction

OVER the past several years, there has been a resurgence of interest in Mars missions, including manned missions. A majority of the proposed scenarios for such missions utilize aerobraking to produce the required velocity decrements upon atmospheric entry at Mars and Earth return.[1-3] A survey of aerobraking and its application to a wide range of missions, including Mars, is presented in Ref. 4. Since the 1960s, our capability to analyze high-energy aerothermodynamic phenomena has advanced significantly. However, questions of the most basic nature concerning the flowfield about large Mars mission vehicles aerobraking into the Earth's atmosphere at very high speeds are still unanswered. In particular, at the point of maximum heating rate during the Earth re-entry of the proposed vehicles, is the flowfield in chemical and/or thermal equilibrium? Answering this question, providing a first look at the characteristics of these flowfields, and examining the capabilities of an existing computational tool with current kinetic models in this high-energy realm are the objectives of the present work.

Figure 1, taken from Ref. 2, presents the atmospheric flight domains of both Mars and Earth entry for selected Mars mission launch windows between the years 2010 and 2025. The maximum heating rate during Earth re-entry occurs around 75-km altitude at 12 km/s (the knee in the curve of Fig. 1).

Several geometric shapes and sizes have been suggested for the Earth aerobrake. Reference 2 suggests a low lift/drag geometry for the Earth re-entry aerobrake similar to that of the Aeroassist Flight Experiment (AFE). The AFE aerobrake is an elliptically capped raked 60-deg cone with a circular aft skirt. Apollo-type aerobrakes have also been suggested. The size of the Earth aerobrake depends greatly on mission strategies. In particular, some strategies require only the return of the human crew and Mars samples; others plan to also salvage reusable spacecraft hardware. Aerobrakes for the crew-only return are small, ranging in base radius from 2 to 6 m. In the present work, a representative axisymmetric body similar to a rotation of one plane of the AFE is examined. This representative body is a spherically capped 60-deg cone with a circular aft skirt. Base radii of 2 and 6 m are examined at 70- and 80-km altitude. The 2-m base radius aerobrake and its computational mesh are shown in Fig. 2. All four cases, graphically depicted by the filled symbols in Fig. 3, have entry speeds of 12 km/s. Binary scaling lines of constant $\rho_\infty R$ have been added to Fig. 3.

Information regarding the state of thermochemical nonequilibrium for the Earth entry of these representative Mars

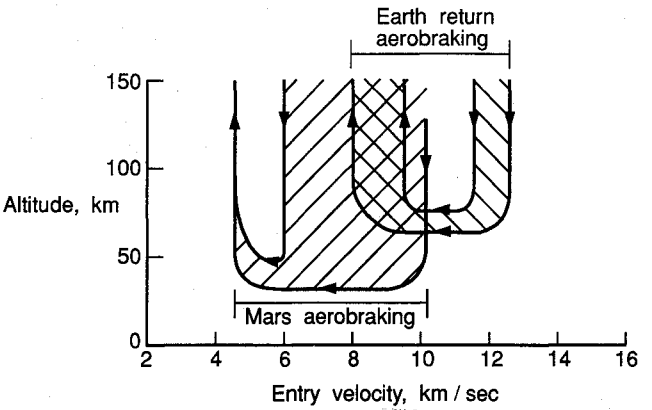

Fig. 1 Atmospheric flight domains for selected Mars missions.

Received May 19, 1990; presented as Paper 90-1698 at the AIAA/ASME 5th Thermophysics and Heat Transfer Conference, Seattle, WA, June 18-20, 1990; revision received Feb. 13, 1991; accepted for publication March 25, 1991.

*Aerospace Engineer, Aerothermodynamics Branch, Space Systems Division. Member AIAA.

†Aerospace Engineer, Aerothermodynamics Branch, Space Systems Division. Senior Member AIAA.

mission vehicles at the aforementioned entry conditions can be estimated from Fig. 4. The equilibrium regions defined in this figure are a compilation of the work of Gupta et al.,[5] which examined the stagnation region of a 0.3-m (1.0-ft) radius sphere using viscous shock layer and Navier-Stokes methods. In the present paper, the base radii of the Earth return aerobrakes are 2 and 6 m with corresponding nose radii of 1.077 and 3.23 m. The principle of binary scaling can be used to scale the ordinate of Fig. 4 to these larger characteristic body dimensions. For instance, a 56.5-km altitude for the 0.3-m-radius sphere becomes a 75-km altitude for a 3.23-m-radius sphere. Thus, the 56.5-km altitude, 12-km/s point on the figure corresponds to 75-km altitude, 12-km/s for the 6-m base radius body. The figure then predicts that the stagnation region of this 6-m body traveling 12 km/s at 75-km altitude will be in thermal equilibrium and chemical nonequilibrium. In addition, the figure indicates that an 11-species air chemistry model is required. Similarly, at 12 km/s and 80-km altitude, the smaller 2-m base radius body with 1.077-m nose radius is estimated to involve significant regions of both thermal and chemical nonequilibrium. From this simple analysis, all four test cases selected should involve chemical nonequilibrium effects. Thermal nonequilibrium is predicted for the 2-m body at 80 km, whereas the 6-m body at 70 km is predicted to be in thermal equilibrium. This figure pertains only to the stagnation region of flow about spheres. Binary scaling predicts a similarity only between the distributions of species whose chemistry is dominated by two-body collisions. This scaling, however, does provide some insight into the trends that should be expected. A full flowfield analysis is required to establish the thermochemical state for the entire flowfield over more realistic aerobrake geometries.

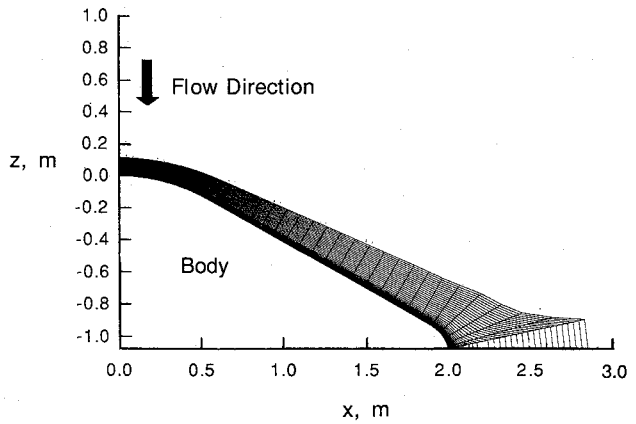

Fig. 2 Representative axisymmetric aerobrake geometry and computational mesh: 2-m base radius body.

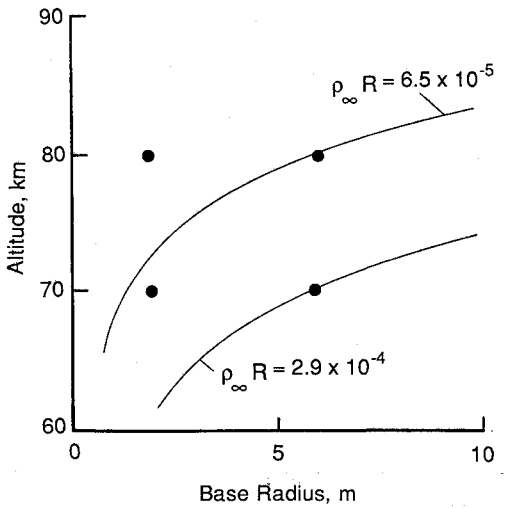

Fig. 3 Four test cases examined at 12 km/s: lines of constant binary scaling coefficient overlaid.

Equilibrium: Thermal, Chemical, Global

A mixture of gases at a point is in local thermal equilibrium when the internal energies of each species form a Boltzman distribution at heavy particle translational temperature T across each of their respective energy spectra. When, for example, the distribution of vibrational energies does not fit the Boltzman distribution for temperature T, thermal nonequilibrium effects are present at that point. The two-temperature approximation of Park[6] assumes that, at such a nonequilibrium location, the distribution of vibrational energies still forms a Boltzman distribution but at a different temperature: the vibrational temperature T_V. Thermal equilibrium follows if $T = T_V$. In a computational fluid dynamics environment, an additional transport equation for the vibrational energy is integrated alongside the gasdynamic equations. In addition to convection and diffusion terms, this equation contains a term that models the finite rate excitation of vibrational modes due to molecular collisions.

A mixture of gases at a point is in local chemical equilibrium when the chemical species concentrations at that point are a function of local pressure and temperature alone. If history effects of convection and diffusion affect local species concentrations, the point is in chemical nonequilibrium. Numerical computation of such a flow requires transport equations for each of the chemical species. Source terms in these equations account for the finite rate production and destruction of species due to chemical reactions. Chemical equilibrium occurs when the chemical reaction rates are significantly faster than the time scales of the local flow and so the species conservation equations reduce to a balance between production and destruction of the species because of chemical reactions. These two definitions define the state of local thermochemical equilibrium at a point in the flowfield.

From the definitions of local equilibrium, a global definition of thermal or chemical equilibrium can be defined. Global equilibrium may be defined as when every point in the

Regions with Chemical Thermal Nonequilibrium	
Region	Aerothermal Equilibrium
Ⓐ	Chemical and thermal equilibrium
Ⓑ	Chemical nonequilibrium with thermal equilibrium
Ⓒ	Chemical and thermal nonequilibrium

Chemical Species in High Temperature Air		
Region	Air Chemical Model	Species Present
Ⓘ	2 species	O_2, N_2
Ⓘⓘ	5 species	O_2, N_2, O, N, NO
Ⓘⓘⓘ	7 species	O_2, N_2, O, N, NO, NO^+, e^-
Ⓘⓥ	11 species	O_2, N_2, O, N, NO, O_2^+, N_2^+, O^+, N^+, NO^+, e^-

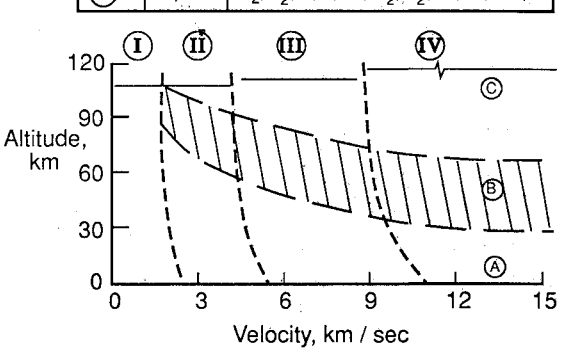

Fig. 4 Stagnation region air chemistry for a 0.3-m-radius sphere (from Ref. 5).

flowfield is in local equilibrium. Under this precise definition, however, no vibrationally excited, chemically reacting flow is in equilibrium since there is always a finite, albeit possibly very small, region where nonequilibrium effects are present. A more useful definition of global equilibrium takes into account the relevant length scales of the flowfield in question. This relevant length scale definition states that a flowfield is in global equilibrium when nonequilibrium effects are restricted to a negligibly small region. The characteristic time scales for the flowfield, the vibrational relaxation process, and the chemical reactions are denoted by t_f, t_v, and t_c. The relevant length scale definition of chemical equilibrium requires $t_c \ll t_f$ everywhere. Similarly, thermal equilibrium requires $t_v \ll t_f$ everywhere. When discussing chemical nonequilibrium, the Damkohler number D is often used:

$$D = t_f/t_c \tag{1}$$

A Damkohler number of order 1 or smaller indicates nonequilibrium chemistry.

Approach

The physical phenomena expected to occur in these high-energy flows are complex. For such Earth return missions, radiative heating will be at least as important as convective heating. In addition, high ablation rates will be necessary.[1] Ablation can introduce radiative blockage due to ablative products and/or turbulent transition due to ablative blowing. Hence, in addition to chemical and vibrational nonequilibrium, the effects of radiation, ablation, and possibly even turbulence must be considered if a detailed flowfield analysis is to be obtained. The primary objective of this work is to establish the state of thermochemical nonequilibrium of such flowfields. Therefore, the added complexities of radiation, ablation, and turbulence are not included in this analysis.

The NASA Langley Aerothermodynamic Upwind Relaxation Algorithm (LAURA) is an upwind-biased point implicit relaxation algorithm for obtaining the numerical solution of the governing equations of viscous hypersonic flows.[7,8] This code has been used to analyze numerous aeroassisted orbital transfer vehicles (AOTVs) including the AFE.[9,10] Further discussion of the LAURA code and its physical models is included in the next section.

Three numerical approaches are utilized to establish the degree of nonequilibrium effects present in the test cases. First, the complete thermochemical nonequilibrium LAURA code is used. Second, by artificially accelerating the thermal relaxation rates, the LAURA code can also produce results in thermal equilibrium with chemical nonequilibrium. Finally, a viscous shock layer (VSL) equilibrium method[11] is used to produce thermochemical equilibrium results. Artificially forcing thermal equilibrium by accelerating the vibrational relaxation rates in LAURA is not the physically correct method of obtaining equilibrium solutions. It does, however, offer a means of isolating thermal equilibrium effects within a single code. By examining the flowfield created by the thermochemical nonequilibrium LAURA code alone and comparing this solution with the other equilibrium results, the four cases examined are found to all involve both thermal and chemical nonequilibrium effects. These effects range from minimal in the larger 6-m base radius body at 70-km altitude to dominant in the smaller 2-m base radius body at 80-km altitude.

Method of Solution

The numerical formulation of the program LAURA is presented in Ref. 7. A description of the physical models within the program appears in Ref. 8.

The 11-species air chemistry model in LAURA solves conservation equations for N, O, N_2, O_2, NO, ions of each, and free electrons. The total equation set consists of 11-species conservation equations, three momentum equations (one of which is extraneous for axisymmetric flow), a total energy equation, and an equation for the vibrational-electronic energy. Reaction source terms in the conservation equations are defined by Park's set of chemical reactions and reaction-rate coefficients.[6] Fully catalytic, constant temperature (1500 K) wall boundary conditions are used in all of the calculations.

The vibrational-electronic energy equation contains terms that model the relaxation processes between energy modes. The vibrational-translational relaxation term in the equation assumes a linear variation of relaxation rate with the difference between vibrational energy defined at T and that defined at T_V (a Launder-Teller relation). The relaxation time is then computed as a blend of the Millikan and White semiempirical correlations[12] with a high-temperature correction suggested by Park.[13] To force a state of thermal equilibrium on the solution, this vibrational-translational relaxation rate is increased by a factor of 10.[6] Though computationally inefficient, this method of producing results in thermal equilibrium (yet still chemical nonequilibrium) is a simple and practical modification of the existing code.

The VSL code of Gupta et al.[11] is used to compute thermochemical equilibrium solutions. Although this code can model coupled radiation and ablation injection, neither of these was used to produce the VSL results presented in this paper. The code has been used in the past to examine the flowfield about the AFE vehicle.[14] The equilibrium version of VSL utilizes the same curve fits as LAURA to establish the thermodynamic and transport properties. Because of the inherent differences between the VSL and LAURA methods, however, solution differences cannot be attributed to the equilibrium assumption only.

Results and Discussion

The representative axisymmetric geometry examined is a spherically blunted 60-deg cone with a circular aft skirt. The ratio of nose radius to skirt radius is 5.0. Base radii of 2 and 6 m are examined. For the 2-m-radius aerobrake, the nose radius is 1.077 m. The 30 × 64 computational grid about this configuration is shown in Fig. 2. There are 30 grid cells along the body. The computational grid is generated analytically to start the calculation. As the flowfield develops, the grid lines tangent to the body are shifted to align the grid with the shock and to assure adequate resolution next to the body (cell Reynolds number at body equal to 1). This shock alignment causes the unusual grid in the region of the exit boundary.

All calculations are for Earth entry speeds of 12 km/s. Both 70- and 80-km geometric altitudes are examined at this velocity for each of the 2- and 6-m base radius bodies (Fig. 3). Freestream density, temperature, and pressure at 70 km are 8.7535×10^{-5} kg/m^3, 219.7 K, and 5.52047 N/m^2, respectively. The density, temperature, and pressure at 80-km altitude are 1.99×10^{-5} kg/m^3, 180.65 K, and 1.0366 N/m^2, respectively.

Chemical nonequilibrium and thermal nonequilibrium issues are discussed separately. Chemical issues are discussed first.

To determine the state of chemical nonequilibrium requires a comparison between the characteristic time scale of the chemical reactions and that of the local flow. When these two time scales are of the same order or the chemical time scale is larger (i.e., Damkohler number of order 1 or smaller), chemical nonequilibrium effects are present. Identifying the correct chemical time scales to compare, however, is not trivial. Eleven-species air chemistry models typically include 40 or more elementary reactions (counting forward and backward reactions separately). There is some ambiguity concerning the definition of chemical time scales from such a complex system of elementary reactions. Computational singular perturbation (CSP)[15] recasts the physical representation of the elementary reaction set into an equivalent reduced set of linearly independent reaction groups. The reaction rate of each reaction group is associated with a *single* eigenvalue. The inverse of this eigen-

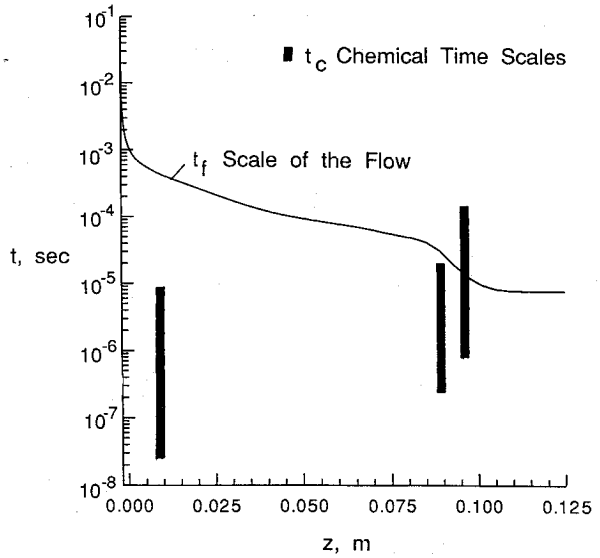

Fig. 5 Computational singular perturbation chemical time scales across stagnation region shock layer for 6-m base radius body at 70-km altitude and 12-km/s velocity.

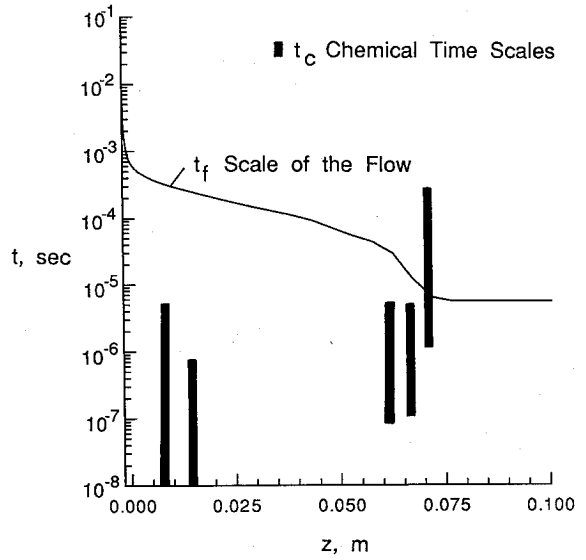

Fig. 6 Computational singular perturbation chemical time scales across stagnation region shock layer for 6-m base radius at 80-km altitude and 12-km/s velocity.

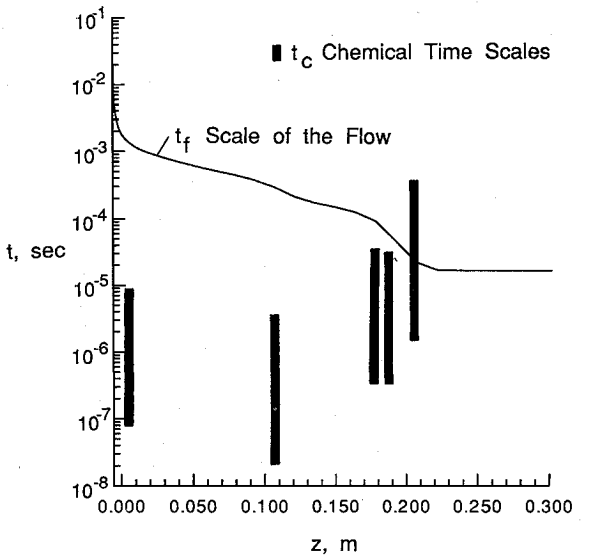

Fig. 7 Computational singular perturbation chemical time scales across stagnation region shock layer for 2-m base radius body at 70-km altitude and 12-km/s velocity.

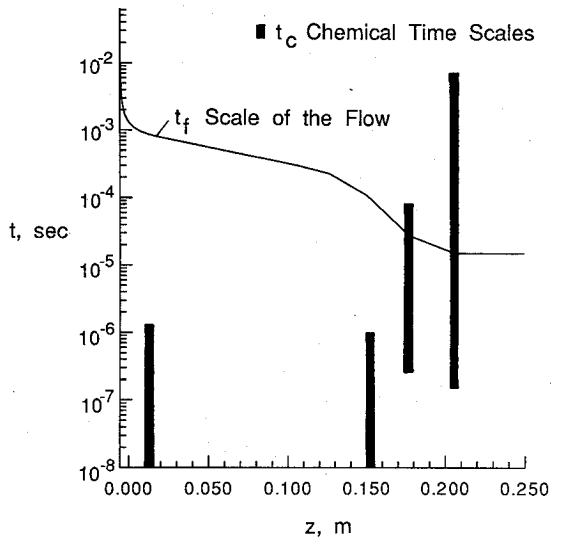

Fig. 8 Computational singular perturbation chemical time scales across stagnation region shock layer for 2-m base radius body at 80-km altitude and 12-km/s velocity.

value is a time scale. The range of slowest to fastest chemical time scales at a point in the flowfield is then the span of the time scales for the reaction group. The CSP method also identifies partial equilibrium relations and quantifies the participation of each elementary reaction with respect to species evolution. (These features are not exploited in the present work.) Figures 5–8 present a comparison of the CSP time scales, represented by the solid vertical bars, with the scale of the local flow along the stagnation streamline. The CSP chemical time scales are computed at several locations across the shock layer. The local flow time scale is defined as the shock standoff distance divided by the local velocity. The important time scale span to examine in each figure is that immediately behind the shock. The shock is indicated by the step-shaped rise in t_f, which results from the normal velocity drop behind the shock. In Figs. 6–8, the crucial time span is the third vertical bar from the right side of the figure. In Fig. 5, it is the second vertical bar from the right. The chemical time scales present immediately behind the shock determine the reaction rate of the numerous reactions that are initiated in this region. Notice that, in all cases except the 6-m base radius body at 70-km altitude (Fig. 8), the largest chemical time scales of these crucial time spans are of the same order of magnitude as the time scale of the flow. In the remaining case, Fig. 8, the largest time scale in the third vertical bar from the right is two orders of magnitude less than the time scale of the flow. Chemical reactions will proceed very rapidly in this case, and chemical nonequilibrium effects should be restricted to a small region behind the shock.

The effect of chemical reaction times in the neighborhood of the shock is revealed in Figs. 9–12. These figures present a comparison of O_2 density profiles across the shock layer at the stagnation line. Three solutions are shown in each figure: the thermochemical nonequilibrium LAURA solution, the LAURA solution in which the thermal relaxation rates have been accelerated to simulate thermal equilibrium while allowing chemical nonequilibrium, and the equilibrium viscous shock layer solution. The equilibrium profiles indicate a rapid dissociation of O_2 behind the shock, whereas the finite rate chemistry solutions require a finite amount of the shock layer to accommodate the dissociation. The extent of chemical nonequilibrium effects in the shock layer ranges from a large percentage in Fig. 9 to a small percentage in Fig. 12.

The LAURA code is a shock-capturing scheme. To define the extent of the nonequilibrium regions requires adequate grid resolution in the neighborhood of the shock. Simultaneously, the boundary layer demands high resolution to resolve steep gradients near the wall. Past grid studies using the LAURA code[8] have revealed that the cell Reynolds number for the grid cells adjacent to the body should be equal to 1, and cell size growth factors should not exceed 1.2. With these restrictions, the original grid created for the 6-m base radius body at 70-km altitude case resulted in large grid spacing (cell spacing equal to 20% of the shock standoff distance) in the shock region. For this case, the conflicting grid resolution requirements prevent simultaneous resolution of the boundary layer and the shock region with a smoothly varying grid of only 64 cells. The grid used to create Fig. 12 sacrificed grid resolution in the boundary layer to provide adequate resolution in the shock region. The disagreement between the nonequilibrium profiles and the equilibrium profiles in the boundary layer is a grid effect. This case when run with adequate grid resolution in the boundary layer displayed agreement in the boundary layer but smeared profiles in the shock region. The remaining three cases involved either lower densities, which allowed larger cells next to the body while still meeting the cell Reynolds number restriction, and/or smaller body dimensions, which decreased the physical domain the grid had to cover.

Pressure distribution along the body is not sensitive to nonequilibrium effects. Though not shown, the pressure distributions computed by the three numerical approaches were in agreement for each test case.

The degree of thermal nonequilibrium effects present in each of the test cases can be examined by comparing the local flow time scale with the characteristic time scale of the vibrational-translational relaxation. A more revealing indicator, however, comes from a comparison of the translational and vibrational temperatures predicted in the nonequilibrium solution. Under the assumption of Park's two-temperature model, thermal equilibrium implies $T = T_V$. To illustrate the location of the thermal nonequilibrium regions, Figs. 13 and 14 present filled contours of the percentage difference of the vibrational temperature T_V from the translational temperature T for the four test cases. The shaded regions within the 0.1 contours in each figure indicate where T_V is at least 10% < T; 10% is selected as a significant difference in the two tempera-

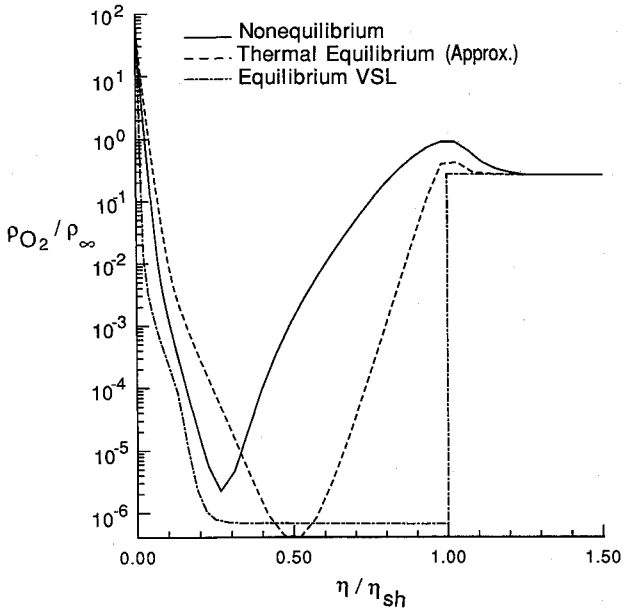

Fig. 9 Comparison of O_2 profiles across stagnation region shock layer for 2-m base radius body at 80-km altitude and 12-km/s velocity.

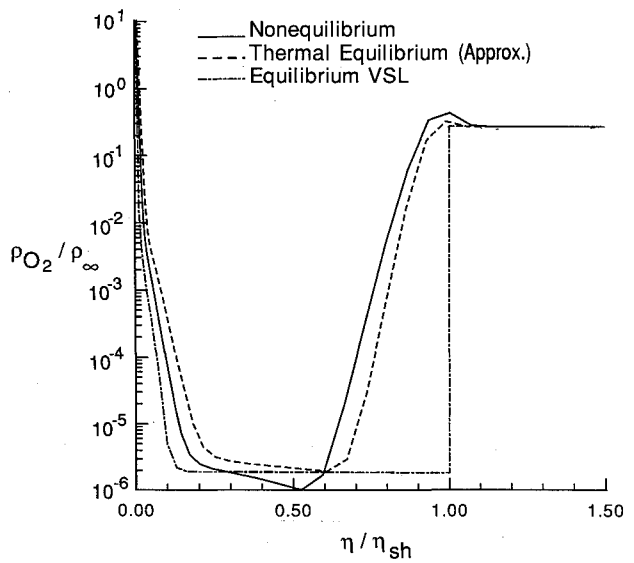

Fig. 10 Comparison of O_2 profiles across stagnation region shock layer for 2-m base radius body at 70-km altitude and 12-km/s velocity.

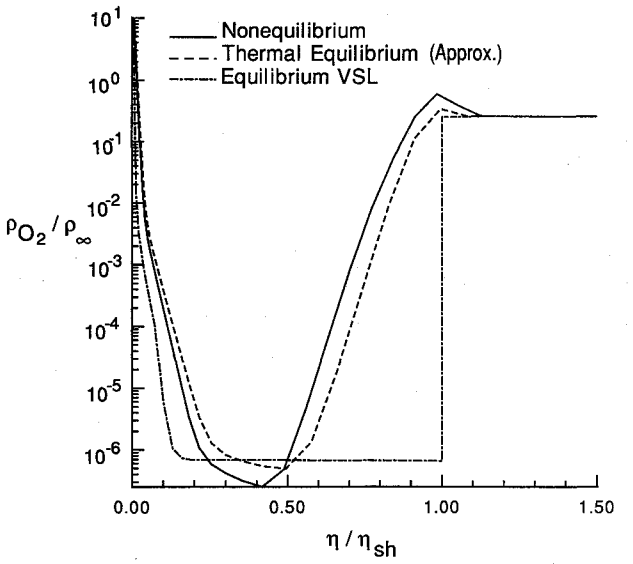

Fig. 11 Comparison of O_2 profiles across stagnation region shock layer for 6-m base radius body at 80-km altitude and 12-km/s velocity.

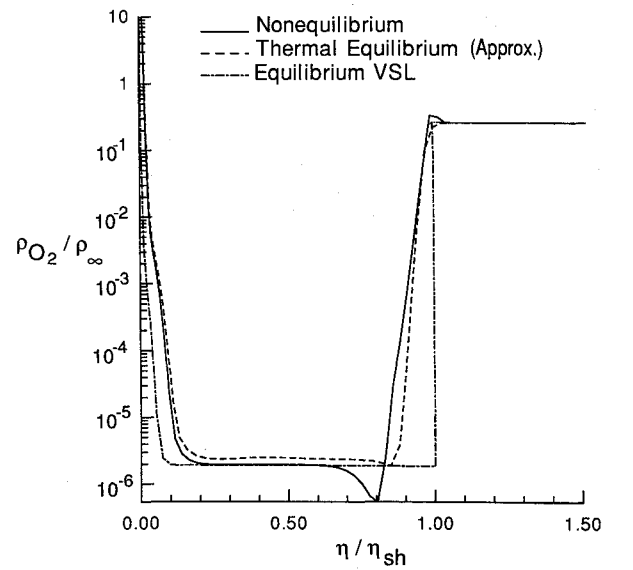

Fig. 12 Comparison of O_2 profiles across stagnation region shock layer for 6-m base radius body at 70-km altitude and 12-km/s velocity.

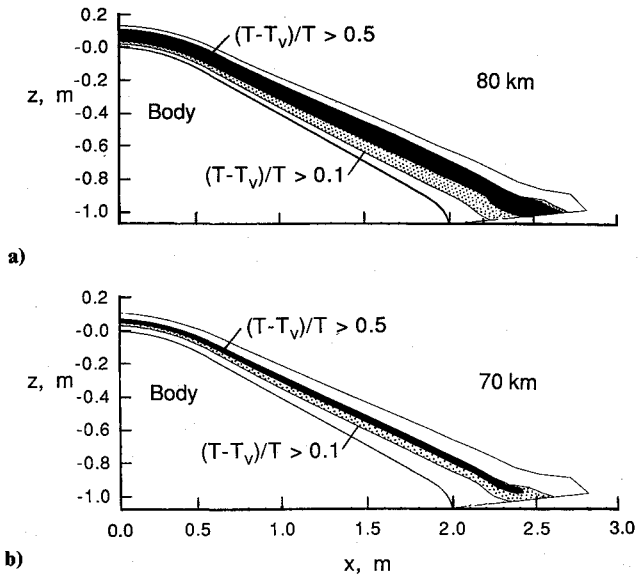

Fig. 13 Contours of percentage difference between vibrational temperature and translational temperature for 2-m base radius body: a) 80 km; b) 70 km.

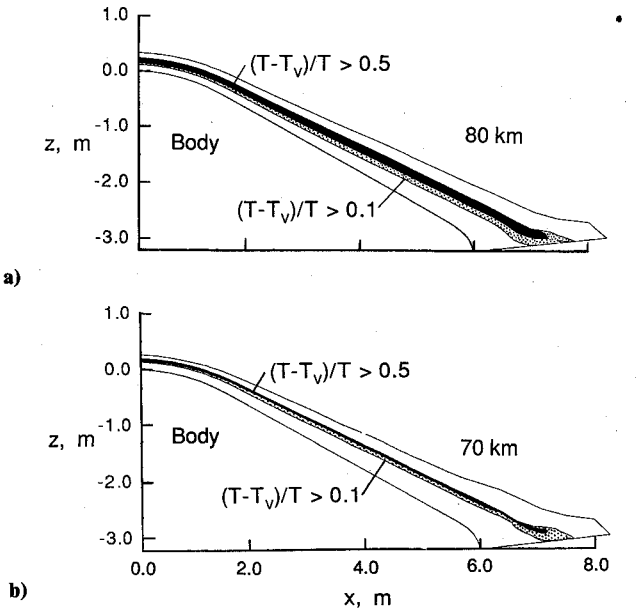

Fig. 14 Contours of percentage difference between vibrational temperature and translational temperature for 6-m base radius body: a) 80 km; b) 70 km.

tures to define the regions involving some thermal nonequilibrium effects. All cases show such temperature differences in the shock region. The solid regions within the 0.5 contours in each figure indicate where T_V is at least 50% < T. The thermal nonequilibrium region covers much of the shock layer for the 2-m-radius 80-km-altitude plot (Fig. 13a). This case is not in thermal equilibrium. Notice the similarity between the 6-m-radius body solution at 80-km altitude (Fig. 14a) and the 2-m-radius body solution at 70 km (Fig. 13b). This similarity indicates that binary scaling, as shown in Fig. 3, can be used to extend solutions over a small range of altitudes and body radii.

Comparison of the nonequilibrium solution temperature profiles with those from the thermal equilibrium solution can give additional information regarding the state of thermal nonequilibrium for each case. Figures 15–18 compare translational temperature and vibrational temperature from the nonequilibrium solution with the translational temperature

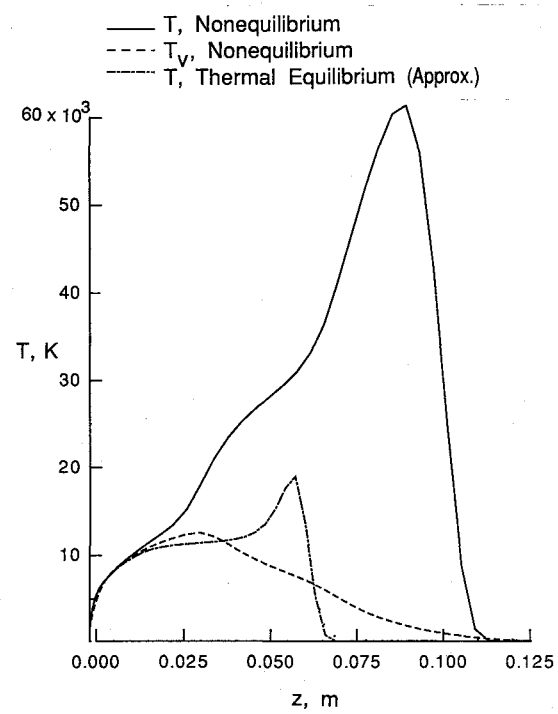

Fig. 15 Comparison of T and T_V stagnation line profiles from the nonequilibrium solution with T from the thermal equilibrium solution for the 2-m base radius body at 80-km altitude.

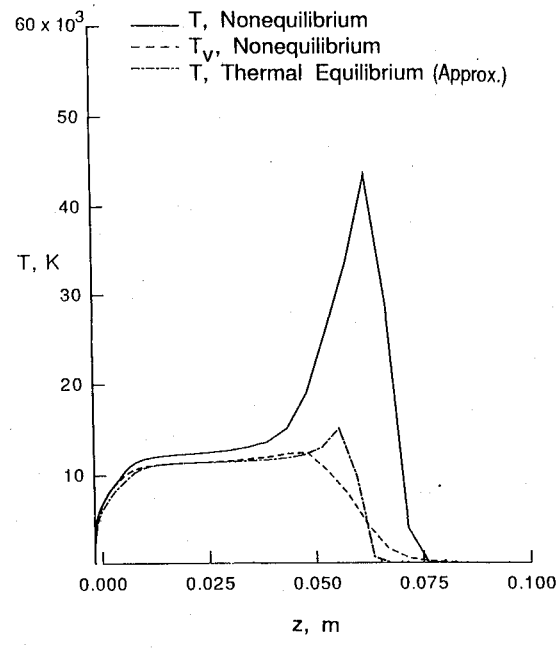

Fig. 16 Comparison of T and T_V stagnation line profiles from the nonequilibrium solution with T from the thermal equilibrium solution for the 2-m base radius body at 70-km altitude.

from the forced thermal equilibrium solution. These profiles for each case show the temperature distribution across the shock layer for the grid cells closest to the stagnation line. Comparing T and T_V from the nonequilibrium solution reveals the same information as presented in Figs. 13 and 14. The temperature profiles display differences in the shock region for all test cases. These differences are greatest in the 80-km, 2-m-body case (Fig. 15). The translational temperature profiles also reveal that shock standoff distance is increased by 80% in the nonequilibrium solution for this case. Again, these results depend on the physical models in LAURA. For such high-energy flows, Park's high-temperature correction for the

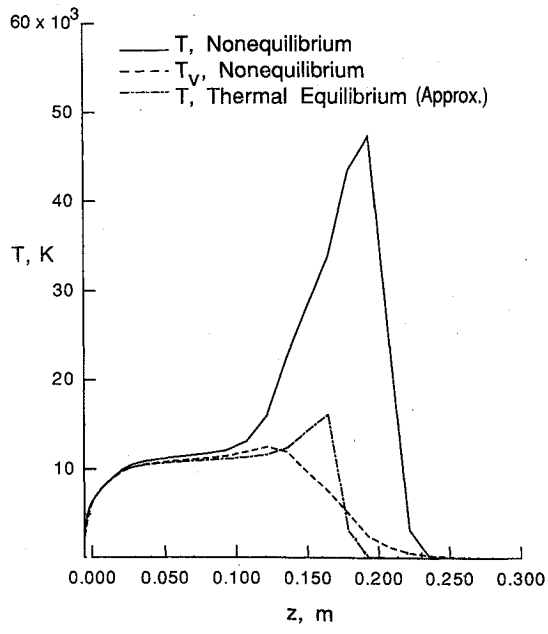

Fig. 17 Comparison of T and T_V stagnation line profiles from the nonequilibrium solution with T from the thermal equilibrium solution for the 6-m base radius body at 80-km altitude.

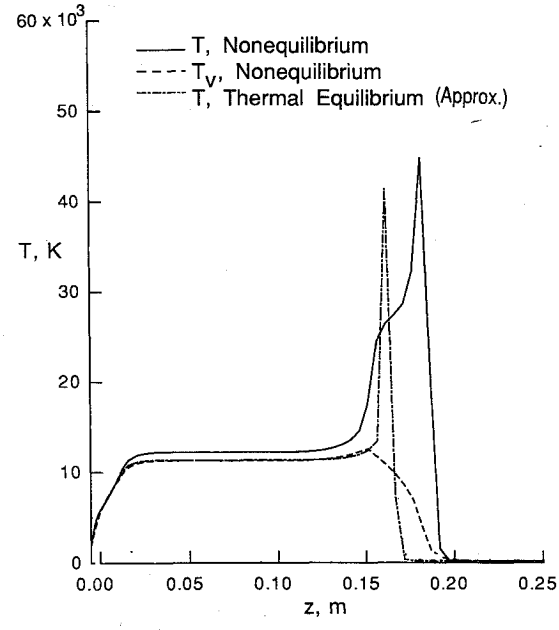

Fig. 18 Comparison of T and T_V stagnation line profiles from the nonequilibrium solution with T from the thermal equilibrium solution for the 6-m base radius body at 70-km altitude.

vibrational relaxation time used in LAURA affects the translational and vibrational temperature profiles. If a larger vibrational-translational energy exchange cross section is used, the vibrational modes will equilibrate more rapidly, and the extent of the vibrational nonequilibrium regions will be reduced.

Conclusions

The thermochemical environment about an axisymmetric 60-deg sphere cone with a circular aft skirt is computed using the NASA Langley Aerothermodynamic Upwind Relaxation Algorithm. Earth entry at 12 km/s is examined at 70- and 80-km altitudes for vehicle base radii of 2 and 6 m. These four test cases bracket some proposed scenarios for Earth re-entry of a manned Mars mission aerobrake at this velocity. Thermochemical nonequilibrium results are examined for each case and compared with thermal equilibrium results produced by artificially accelerating vibrational relaxation rates and with equilibrium results produced by a viscous shock layer method. Forcing equilibrium by artificially accelerating the vibrational relaxation processes proved to be a feasible but computationally expensive technique. In general, equilibrium solutions should be computed with the appropriate equation set.

From an examination of chemical time scales predicted by computational singular perturbation and solution O_2 profiles, all four cases are shown to contain some chemical nonequilibrium effects. Comparisons of translational and vibrational temperatures reveal that all cases also involve thermal nonequilibrium effects. These effects, however, are minimal in the 6-m base body at 70-km altitude. This largest body at lowest altitude is near chemical and thermal equilibrium. The smallest body, base radius of 2 m, at the higher altitude, 80 km, has regions dominated by both thermal and chemical nonequilibrium effects. The remaining two cases, the 6-m base body at 80-km altitude and the 2-m base body at 70-km altitude, lie near a line of constant binary scaling parameter. These two cases involve significant regions of chemical nonequilibrium and, to a lesser degree, thermal nonequilibrium. The binary scaling line between these two cases approximates the interface above which both thermal and chemical nonequilibrium effects are dominant. No interface between thermochemical equilibrium and chemical nonequilibrium (with thermal equilibrium) was obvious from the results examined.

The conflicting needs of adequate grid resolution in the boundary layer and in the shock region necessitate more than 64 grid cells in the normal direction for the 6-m body at 70-km altitude test case when cell size growth factor is restricted to 1.2. The degree of nonequilibrium present in these test cases depends on the physical models in the algorithm. In-depth grid refinement studies and parametric variation of the physical models are required if a more exact definition of the extent of nonequilibrium regions is required.

Acknowledgments

The authors are grateful to R. N. Gupta of Scientific Research and Technology, Inc., Hampton, Virginia, for providing the viscous shock layer solutions, and D. Goussis of Princeton University for supplying the computational singular perturbation time scales.

References

[1]Walberg, G. D., " A Review of Aerobraking for Mars Missions," International Astronautical Federation, Paper 88-196, Oct. 1988.

[2]Braun, R. D., "A Survey of Interplanetary Trajectory Options for a Chemically Propelled Manned Mars Vehicle," American Astronautical Society, Paper 89-202, April 1989.

[3]Menees, G. P., "Aeroassisted-Vehicle Design Studies for a Manned Mars Mission," NASA TM-100031, Oct. 1987.

[4]Walberg, G. D., "A Survey of Aeroassisted Orbit Transfer, *Journal of Spacecraft and Rockets,* Vol. 22, No. 1, 1985, pp. 3-18.

[5]Gupta, R. N., Yos, J. M., Thompson, R. A., and Lee, K. P., " A Review of Reaction Rates and Thermodynamic and Transport Properties for the 11-Species Air Model for Chemical and Thermal Nonequilibrium Calculations to 30000 K," NASA RP-1232, Aug. 1990.

[6]Park, C., "Assessment of Two-Temperature Kinetic Model for Ionizing Air," AIAA Paper 87-1574, June 1987.

[7]Gnoffo, P. A.,"Upwind-Biased Point-Implicit Relaxation Strategies for Viscous, Hypersonic Flows," AIAA Paper 89-1972, June 1989.

[8]Gnoffo, P. A., Gupta, R. N., and Shinn, J. L., "Conservation Equations and Physical Models for Hypersonic Air Flows in Thermal and Chemical Nonequilibrium," NASA TP-2867, Feb. 1989.

[9]Gnoffo, P. A., and Greene, F. A., "A Computational Study of the Flowfield Surrounding the Aeroassist Flight Experiment Vehicle," AIAA Paper 87-1575, June 1987.

[10]Gnoffo, P. A., "Application of Program LAURA to Three-Dimensional AOTV Flowfields," AIAA Paper 86-0565, Jan. 1986.

[11]Gupta, R. N., Sutton, K., Moss, J. N., and Lee, K. P., " Viscous Shock Layer Solutions with Coupled Radiation and Ablation Injection for Earth Entry," AIAA Paper 90-1697, June 1990.
[12]Millikan, R. C., and White, D. R., " Systematics of Vibrational Relaxation," *Journal of Chemical Physics,* Vol. 39, No. 12, 1963, pp. 3209–3213.
[13]Park, C., "Problems of Rate Chemistry in the Flight Regimes of Aeroassisted Orbital Transfer Vehicles," *Thermal Design of Aeroassisted Orbital Transfer Vehicles,* edited by H. F. Nelson, Vol. 96, Progress in Astronautics and Aeronautics, AIAA, New York, 1985, pp. 511–537.
[14]Gupta, R. N., "Stagnation Flowfield Analysis for an Aeroassist Flight Experiment Vehicle," AIAA Paper 88-2613, June 1988.
[15]Goussis, D., Lam, S., and Gnoffo, P., "Reduced and Simplified Chemical Kinetics for Air-Dissociation Using Computational Singular Perturbation," AIAA Paper 90-0644, Jan. 1990.

James E. Daywitt
Associate Editor